Evaluation of novel KEK/HPK n-in-p pixel sensors for ATLAS upgrade with testbeam

R. Nagai [a],*, J. Idárraga [b], C. Gallrapp [c], Y. Unno [d], A. Lounis [b], O. Jinnouchi [a], Y. Takubo [d], K. Hanagaki [e], K. Hara [f], Y. Ikegami [d], N. Kimura [g], K. Nagai [f], I. Nakano [h], R. Takashima [i], S. Terada [d], J. Tojo [j], K. Yorita [g], S. Altenheiner [n], M. Backhaus [r], M. Bomben [l], D. Forshaw [p], M. George [m], J. Janssen [r], J. Jentzsch [n], T. Lapsien [n], A. La Rosa [q], A. Macchiolo [k], G. Marchiori [l], C. Nellist [s], I. Rubinsky [o], A. Rummler [n], G. Troska [n], P. Weigell [k], J. Weingarten [m]

[a] Department of Physics, Tokyo Institute of Technology, 2-12-1 Ookayama, Meguro-ku, Tokyo 152-8550, Japan
[b] Laboratoire de l'Accélérateur Linéaire (LAL), Université Paris-Sud XI, Plateau du Moulon, 91400 Orsay, France
[c] European Organization for Nuclear Research (CERN), CH-1211 Genève 23, Switzerland
[d] Institute of Particle and Nuclear Study, High Energy Accelerator Research Organization (KEK), 1-1 Oho, Tsukuba-shi, Ibaraki 305-0801, Japan
[e] Department of Physics, Osaka University, Machikaneyama-cho, Toyonaka-shi, Osaka 560-0043, Japan
[f] Institute of Pure and Applied Sciences, University of Tsukuba, 1-1-1 Tennoudai, Tsukuba-shi, Ibaraki 305-8571, Japan
[g] Research Institute for Science and Engineering, Waseda University, Japan
[h] Department of Physics, Okayama University, 3-1-1 Tshushima-naka, Kita-ku, Okayama-shi, Okayama 700-8530, Japan
[i] Department of Education, Kyoto University of Education, 1 Fukakusa-Fujimori-cho, Fushimi-ku, Kyoto 612-8522, Japan
[j] Department of Physics, Kyushu University, 6-10-1 Hakozaki, Higashi-ku, Fukuoka 812-8581, Japan
[k] Max-Planck-Institut für Physik, Föhringer Ring 6, 80805 München, Germany
[l] Laboratoire de Physique Nucleaire et de Hautes Énergies (LPNHE), Barre 12-22, 1er étage - 4 place Jussieu - 75252 Paris Cedex 05, France
[m] II. Physikalisches Institut, Georg-August-Universität Göttingen, Friedrich-Hund-Platz 1, 37077 Göttingen, Germany
[n] Technische Universität Dortmund, Experimentelle Physik IV, 44221 Dortmund, Germany
[o] Deutsches Elektronen-Synchrotron (DESY), Notkestraße 85, 22607 Hamburg, Germany
[p] Department of Physics, The University of Liverpool, L69 7ZE Liverpool, United Kingdom
[q] Section de Physique (DPNC), Université de Genève, 24 quai Ernest Ansermet 1211 Genève 4, Switzerland
[r] University of Bonn, Physikalisches Institut, Nussallee 12, D-53115 Bonn, Germany
[s] University of Manchester, School of Physics and Astronomy, Oxford Road, Manchester M13 9PL, United Kingdom

ARTICLE INFO

ABSTRACT

A new type of n-in-p planar pixel sensors have been developed at KEK/HPK in order to cope with the maximum particle fluence of $1–3 \times 10^{16}$ 1 MeV equivalent neutrons per square centimeter (n_{eq}/cm^2) in the upcoming LHC upgrades. Four n-in-p devices were connected by bump-bonding to the new ATLAS Pixel front-end chip (FE-I4A) and characterized before and after the irradiation to 2×10^{15} n_{eq}/cm^2. These planar sensors are 150 μm thick, using biasing structures made out of polysilicon or punch-through dot and isolation structures of common or individual p-stop. Results of measurements with radioactive ^{90}Sr source and with a 120 GeV/c momentum pion beam at the CERN Super Proton Synchrotron (SPS) are presented. The common p-stop isolation structure shows a better performance than the individual p-stop design, after the irradiation. The flat distribution of the collected charge in the depth direction after the irradiation implies that the effect of charge trapping is small, at the fluence, with the bias voltage well above the full depletion voltage.

© 2012 Published by Elsevier B.V.

1. Introduction

The High Luminosity LHC (HL-LHC) upgrade is planned for 2022 in order to extend the discovery potential for new physics and improving the data statistics for high precision measurements.

Its specifications include an increased peak luminosity of up to 5×10^{34} cm^{-2} s^{-1}, and a total integrated luminosity of 3000 fb^{-1} which represents a five times larger peak and a 10 times higher integrated luminosity than foreseen for the current ATLAS detector [1].

Once such upgraded run starts, the present ATLAS Pixel detectors [2] might sustain elevated radiation damage from the maximum particle fluence of $1–3 \times 10^{16}$ 1-MeV equivalent neutrons per square centimeters (n_{eq}/cm^2) for the innermost layer. The increased luminosity will make it necessary to implement a new

* Corresponding author.
E-mail address: nagai@hep.phys.titech.ac.jp (R. Nagai).

pixel detector which is able to cope with the increased occupancy and the fluence. Several different sensor technologies have been proposed to instrument the upgraded ATLAS Pixel detectors, as for example, silicon 3D [3], silicon planar [4–6], and diamond pixel [7] detectors. In this paper, we present an evaluation of the novel n-in-p planar sensors manufactured by Hamamatsu Photonics (HPK) in collaboration with KEK et al. [8,9].

The n^+ readout in the p-type silicon bulk (n-in-p type) has a number of advantages over the conventional n-type sensors [10]. The n^+ readout is always formed in the pn-junction side because the type of the bulk does not invert even if high radiation damage is sustained. This makes it possible the operations without full depletion, thus highly radiation tolerant. It allows to achieve a higher charge collection efficiency, by collecting fast electron carriers in the strong electric field in the junction side, thus the trapping effects in the bulk material, which are expected to increase with the radiation damage, could be reduced [11]. The single sided lithographic process is expected to reduce fabrication cost thus allowing larger detector coverage with pixel sensors. On the other hand, the n-in-p sensors have additional requirements e.g. the need for an inter-pixel isolation and the coating of the sensor edges, where a high bias is present, to prevent sparks with the chip at ground potential [9].

2. n-in-p sensor design

The three sensor designs examined are illustrated in Fig. 1: the common p-stop and the polysilicon resistor (PolySi), the individual p-stop and PolySi, and the individual p-stop and the punch-through dot (PTLA) [9]. The n-in-p sensor requires an isolation structure to intercept the inversion layer between neighboring n^+ pixels due to the positive charge-up in the surface interface of the silicon and the oxide. A bias structure is implemented to bias the pixels for testing the sensors prior to the bump-bonding to the readout electronics. The structure has to have a resistance high enough to isolate the pixels and to minimize the parallel noise.

The common p-stop has only one p-stop line for all pixels, which runs through adjacent pixels. The individual p-stop has an isolated p-stop line for each pixel, thus the pixel size is slightly
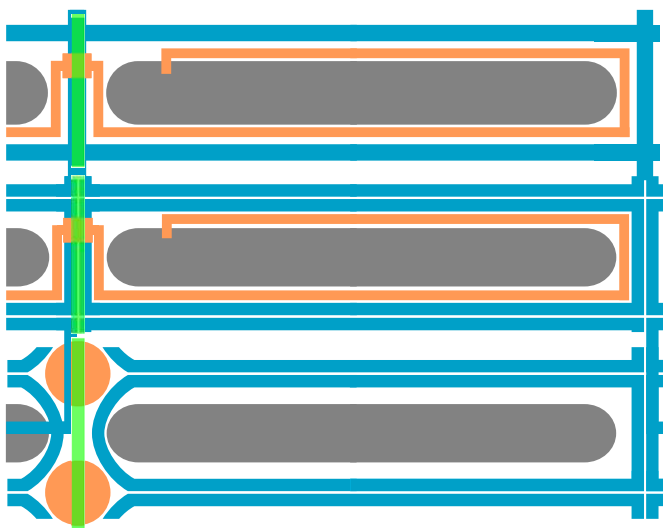

Fig. 1. Designs of the n-in-p pixel structure (top: SCC94 and SCC95, middle: SCC93, bottom: SCC96). A pixel implant is shown in the centers, being isolated with common p-stop (top) or individual p-stop (middle and bottom) structure. A bias rail, running vertically in the left side, provides the reference ground voltage to two adjacent pixels through the polysilicon resistor (top and middle) or the punch-through dot (bottom).

Table 1
The properties of the KEK/HPK n-in-p pixel sensors.

Silicon crystal	p-type FZ, 4−7 kΩ cm			
Sensor thickness	150 μm			
Pixel size	50 μm × 250 μm			
ID	Bias st.	Isolation st.	First test	Second test
SCC93	PolySi	Individual p-stop	NR	IR(N/A)
SCC94	PolySi	Common p-stop	NR	NR
SCC95	PolySi	Common p-stop	NR	IR
SCC96	PTLA	Individual p-stop	NR	IR

SCC, single chip card; st., structure; PolySi, polysilicon resister; PTLA, punch-through dots; NR, unirradiated; IR, irradiated to 2×10^{15} n_{eq}/cm^2; N/A, not available.

smaller than in the common p-stop in order to create space for two p-stop lines. The punch-through dot has an implant on silicon bulk from the bias rail. Neither the PolySi nor the bias rail has an implant underneath it. We needed the PTLA dots, not at every four-corner of the pixels, but at alternate four-corner, as one dot acts for the surrounding 4 pixels.

3. Devices under tests and experimental setup

Table 1 shows the properties of the KEK/HPK pixel sensors. The pixel sensors were bump bonded to FE-I4A readout chips [12] and mounted on the single-chip test card (SCC). In 2011, two beamtests [13] were held at H6 beam line of the CERN super proton synchrotron (SPS), using 120 GeV π^+ particles at an average trigger rate of ~ 650 Hz per cycle. The EUDET telescope, composed of six planes, was used for tracking beam particles [14], with a pointing resolution of $\sigma \sim 3$ μm. In the first beamtest, all samples were unirradiated (NR). Afterwards, three samples, SCC93, SCC95 and SCC96, were irradiated at Karlsruhe to 2×10^{15} n_{eq}/cm^2 with 23 MeV protons. In the second beamtest, after irradiation, SCC93-IR developed a data-acquisition problem and was removed from the beam, thus the results after irradiation are based on the measurements of SCC95-IR and SCC96-IR. SCC95-IR and SCC96-IR were also measured with a collimated ^{90}Sr β source in the laboratory with an external trigger.

During the beamtests the samples were characterized with particles imprinting at normal incidence and at 4° angle. The test using a normal incidence angle aimed to understand the efficiency and the charge collection for the samples before and after irradiation. The measurements at small grazing angle allowed to understand the charge collection in the depth of the sensor.

Table 2 shows the run conditions. The threshold of each pixel of the FE-I4A was tuned to a threshold of either 1600 e or 3200 e, while the time-over-threshold (ToT) value was tuned to five for a charge of 10 ke. As there is no reliable ToT to charge calibration available for the FE-I4A chip, at the time of this paper, all quoted charges are given in ToT. Although there is a certain amount of uncertainty between the measurements of the samples, we note that the measurements within one sample using the same tuning are not affected by this uncertainty. In this analysis, dead (no hit) and noisy (occupancy $> 10^{-3}$) pixels were masked. The occupancy was defined as number of random hits per pixel per trigger.

4. Results

4.1. Results for normal incidence angle

Fig. 2 shows the overall tracking efficiency (global) for each sensor as a function of the bias voltage. We defined the efficiency

Table 2
Run conditions (bias voltage, threshold (Th), temperature (T) and ToT for 10 ke (ToT)) of the beam (first and second) and laboratory (lab) tests.

Period	Bias voltage (V)	Th (e)	T (°C)	ToT
Lab	100, 200, 400, 500 600, 800, 1000	1600	−30	5
First	15, 25 50, 75, 100, 125, 150	1600 3200	+20	5
Second	50, 100, 200, 300 400, 500, 600, 700 800, 900, 1000	1600	−40	5

Table 3
The global tracking efficiencies of non-irradiated and irradiated sensors from the first and the second beamtest. The run conditions are summarized in Table 2.

ID	First beamtest	Second beamtest
SCC93	99.7 ± 0.01% (NR)[a]	N/A
SCC94	98.7 ± 0.01% (NR)[a]	99.6 ± 0.01% (NR)[b]
SCC95	99.7 ± 0.01% (NR)[a]	95.6 ± 0.02% (IR)[c]
SCC96	94.2 ± 0.02% (NR)[a]	94.9 ± 0.02% (IR)[c]

[a] Weighted averages and errors of (100, 125, 150 V).
[b] Weighted averages and errors of (100, 200, 300 V).
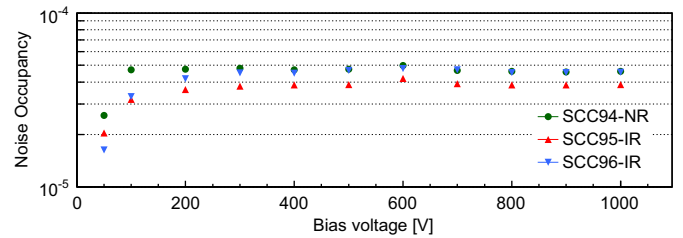[c] Weighted averages and errors of (800, 900, 1000 V).

Fig. 2. The global tracking efficiencies of non-irradiated (NR) and irradiated (IR : 2×10^{15} n_{eq}/cm^2) sensors as a function of the bias voltage. The run conditions are summarized in Table 2.

Fig. 3. The noise occupancies of non-irradiated and irradiated sensors as a function of the bias voltage from the second beamtest.
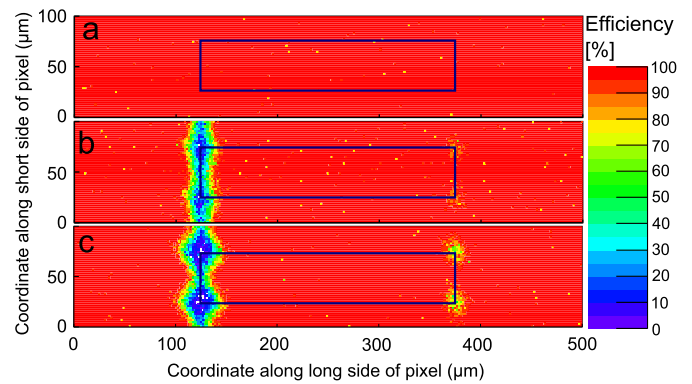

Fig. 4. Local tracking efficiency maps of a pixel of non-irradiated (NR) and irradiated (IR) sensors: (a) SCC94-NR at a bias voltage of 600 V, (b) SCC95-IR at 1000 V and (c) SCC96-IR at 1000 V. The box shows the region of a pixel.

by the existence of a hit within a window of ±1-pixel size in both row and column directions from the track position extrapolated from the EUDET tracking. The non-irradiated sensors showed an efficiency plateau above 25 V and the irradiated ones above 200 V. The non-irradiated, SCC94-NR, recorded an efficiency of 99.8 ± 0.01% when the devices was biased at 200 V and the front-end chip was tuned at a threshold of 1600 e, and the irradiated ones, SCC95-IR and SCC96-IR, recorded efficiencies of 95.7 ± 0.03% and 95.0 ± 0.03% at 1000 V, respectively. Table 3 summarizes the global tracking efficiencies from the first and the second beamtest. The values are weighted averages and errors of three bias voltages in the footnote of the table.

The efficiencies in the central region of a pixel (150 μm < X < 350 μm) were 98.7 ± 0.01% and 99.5 ± 0.01% at a bias voltage of 1000 V for SCC95-IR and SCC96-IR, respectively. SCC95-IR was noisy in the data taking, plausibly due to the readout chip and readout chain.

Fig. 3 shows the noise occupancies obtained from the beamtest data. The noise occupancy represents the number of noise hits per pixel, per trigger. All hits outside the window of ±2 pixel sizes from the track position and the window of the trigger timing (LVL1) of 3 < LVL1 < 10 were accumulated as noise hits, per sensor. The noise hits were then divided by the number of total triggers and the number of active pixels. The noise occupancies were approximately 4×10^{-5} both in the non-irradiated and irradiated sensors. The decrease of the occupancy below 200 V in the non-irradiated sensors may indicate that the most of the hits were caused by the real particles.

Fig. 4 shows the local tracking efficiency maps within a pixel of the unirradiated sensor, SCC94-NR, at 600 V and within the two irradiated sensors, SCC95-IR and SCC96-IR, at 1000 V. The pixels in a sensor were folded into a pixel in the center and adjacent ones. The average number of entries per map-point was approximately 30. The unirradiated sample SCC94-NR in Fig. 4(a) shows an efficiency of ~99%. Similar results were achieved for SCC95-NR before irradiation, which has the same design as SCC94. The irradiated sensors, SCC95-IR and SCC96-IR, indicate an efficiency

of ~99% in the central region but with two larger regions of decreased efficiency at the left corners. In addition, SCC96-IR shows a decreased efficiency in the right corners of the pixel due to the individual p-stop structures.

Fig. 5 shows the charge collection as a function of the bias voltage for SCC95 and SCC96, before and after irradiation. The amount of collected charge may be decreased after irradiation. The collected charge saturates for the unirradiated and irradiated samples at voltages above 50 V and 400 V, respectively. They were also confirmed by the measurements performed in laboratory by using a ^{90}Sr β-source. The full depletion voltages were estimated to be 44 ± 10 V and 380 ± 70 V [9]. The effective doping concentrations were, then, derived to be $(2.6 \pm 0.6) \times 10^{12}$ and $(2.2 \pm 0.4) \times 10^{13}$ cm^3, before and after irradiation, respectively.

Fig. 6 shows the charge collection maps for the unirradiated, SCC94-NR, and the two irradiated sensors, SCC95-IR and SCC96-IR. The charge at the track position is the induced charge in the center pixel. For SCC95-IR sample which has the common p-stop structure with polysilicon bias resistor, the charge collection maps show that it has slightly less tail into the adjacent pixels than SCC96-IR which has the individual p-stop structure with punch-through dots. The larger tail into the adjacent pixels implies a larger charge sharing.
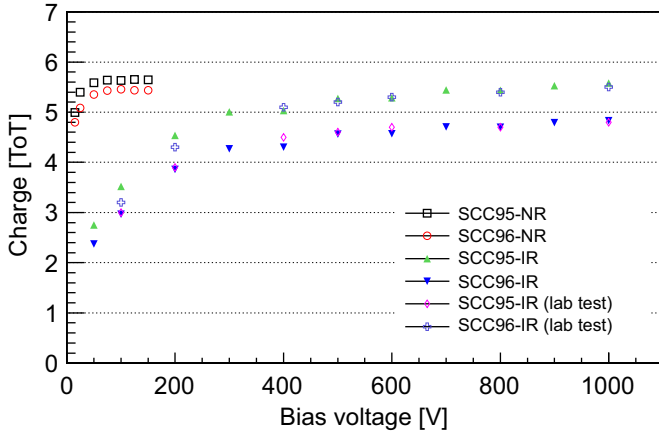
Fig. 5. Charge collection in units of ToT of non-irradiated (NR) and irradiated (IR) sensors as a function of the bias voltage. The run conditions are summarized in Table 2.
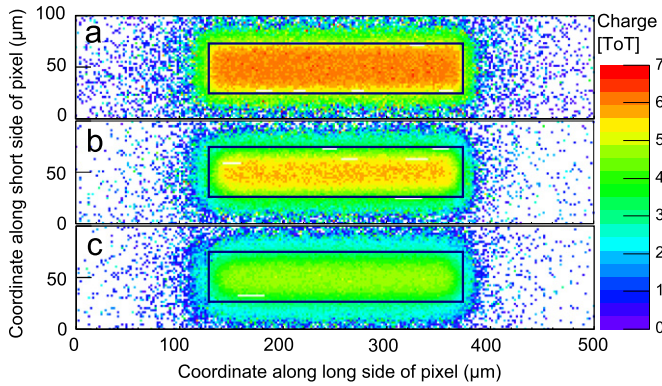

Fig. 6. Charge collection map in a pixel of non-irradiated (NR) and irradiated (IR) sensors: (a) SCC94-NR at a bias voltage of 200 V, (b) SCC95-IR at 1000 V and (c) SCC96-IR at 1000 V. The box shows the region of a pixel.
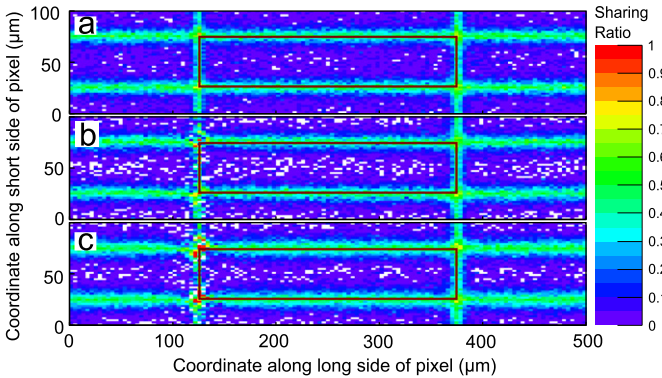

Fig. 7. Local charge sharing map of a pixel of non-irradiated (NR) and irradiated (IR) sensors: (a) SCC94-NR at a bias voltage of 200 V, (b) SCC95-IR at 1000 V and (c) SCC96-IR at 1000 V. The box shows the region of a pixel.

Fig. 7 shows the charge sharing maps. The charge sharing ratio is the ratio of the charge of the pixel at the track position being divided by the sum of the charges of all pixels in the cluster. A slightly wider charge sharing in SCC96-IR is observed in Fig. 7(c) than in SCC95-IR in Fig. 7(b).

4.2. Results for 4° incidence angle

Measurements with a nominal angle of 4° were performed to study the depletion and the charge collection in the depth of the sensor. In the n^+-in-p sensor, the depletion region extends from the n^+ readout side to the back-side. As it reaches the back-side, while increasing the bias voltage, the detector is said to be fully depleted. The electron–holes created in the depleted region generate the induced current in the electrode to be amplified.

In this setup, the track passes along the long side of the pixel and spans 7–9 pixels, giving tracks of up to 2.25 mm. The peak of the cluster size corresponded to the depth of 150 μm. In this way, one can have configurations where a track goes through an undepleted region, which results in a loss of charge collection efficiency or, in the most dramatic case, a non-reactive pixel. At the same time, the depletion depth can be estimated.

Fig. 8 shows a schematic view of the setup where the samples, SCC94-NR and SCC95-IR, are located back to back. In a second comparison, the sensor, SCC96, before and after irradiation is considered as well. Although clusters which were associated with the reconstructed tracks with the telescope were used, neither precision entry- nor exit-coordinate was used for the analysis.

Fig. 9 shows the collected charges in the depth direction for SCC94-NR and SCC95-IR at different bias voltages, and Fig. 10 for SCC96-NR and SCC96-IR. The depth is measured from the charge-collecting side, i.e., n^+ side.

The first-to-second pixel behavior can be best understood in Fig. 9(e): SCC94 at 200 V and SCC95-IR at 1000 V. In the second pixel, the collected charge is $Q \approx 7.4$ ToT, a value 40% higher than the first pixel. The particle enters the first pixel at any point in the surface with a flat probability distribution as the beam is homogeneously distributed in all the sensor, thus the distance traversed is half of the pixel, in average. At the nominal 4°, with a long pixel size of 250 μm, the mean distance traversed in the first pixel is ≈ 130 μm. This is also true for the last pixel in the track. In the inner pixels, the particle traverses ≈ 259 μm of silicon (Si), always. Hence, the charge collected in the first and the last pixel can be, in average, as low as half the charge in the second pixel. The effect of the threshold and trapping modifies this ratio.

The charge Q in the depth direction was calculated by using the normalized pixel responses. In each sensor and at each bias voltage, the responses of each pixel were normalized such that the mean value of the ToT's of the pixel was equal to the mean value of all pixels. We assigned systematic errors to the normalized responses in a pixel to be the square-root of the product of the standard deviation of the overall ToT distribution and the deviation of the responses of the pixel from the mean value.

In Fig. 9(b), SCC94-NR at 10 V and SCC95-IR at 100 V, one can clearly see that SCC94-NR presents a dramatic loss in charge collection at about 90 μm depth and eventually the last two pixels toward the back-side are inactive. One can calculate the depletion depth using the relation $D = \sqrt{2\epsilon(V+V_{bi})/Ne}$ [15], where $\epsilon = 1$ pF/cm is the dielectric constant in Si, V is the bias voltage, V_{bi} is the built-in voltage (≈ 0.5 V), N is the doping concentration which is approximately 2.6×10^{12} cm^{-3} for this sensor, and e is the electron charge. The depth, D, is ≈ 72 μm at $V = 10$ V. This result is comparable with what we observe experimentally within the uncertainty. In the same figure, SCC95-IR at 100 V, presents the same behavior but at a shallower distance, ≈ 70 μm. It contains as well at least three completely inactive pixels. The distance is consistent with the doping concentration of 2.2×10^{13} cm^{-3} and the bias voltage of 100 V.
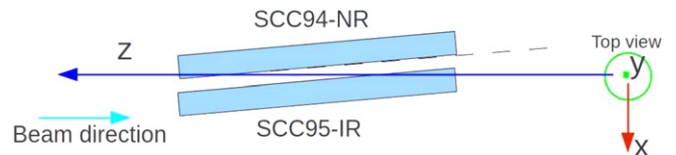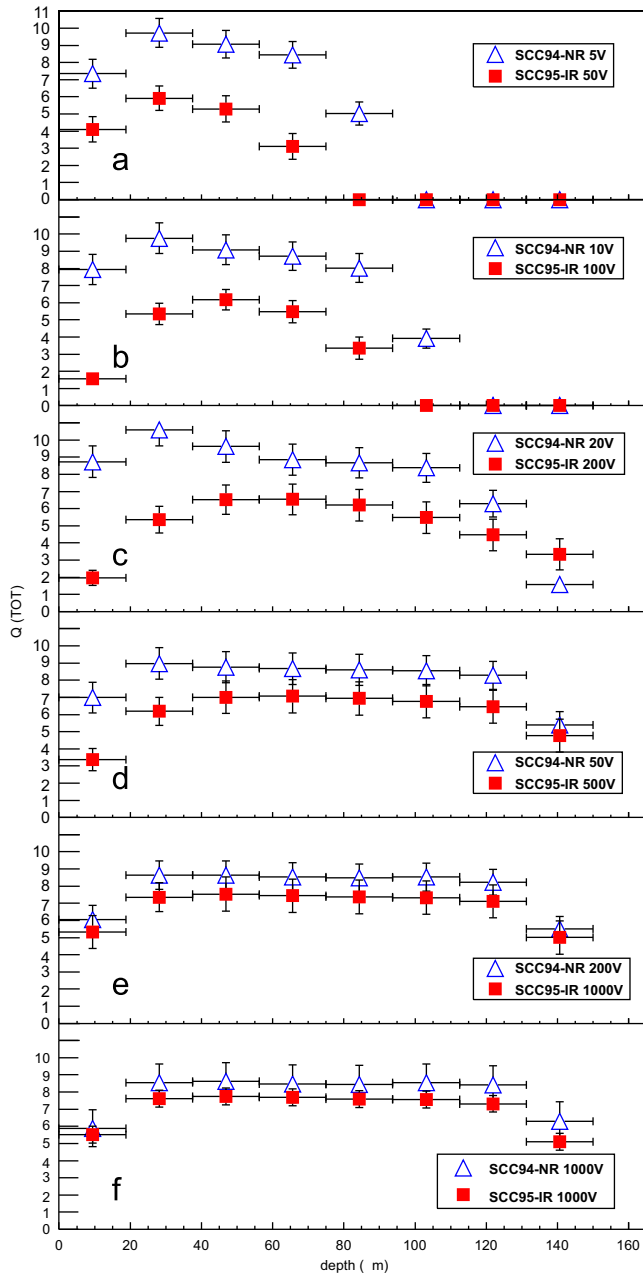

Fig. 8. Schematic of the beamtest setting.

Fig. 9. Comparison of the amount of collected charge between the unirradiated sample SCC94-NR and the irradiated sample SCC95-IR.

Fig. 10. Comparison of the amount of collected charge as a function of depth for SCC96-NR and SCC96-IR.

box gives the cluster size in the most populated entry. The top and bottom edges of the box represent the cluster size with entries greater and smaller than 10% of the center. The solid vertical lines show the tails of the distribution where the entry ends. We observe that the full depletion where the cluster size arrives to its plateau arrives at 50 V for SCC94-NR and about 500 V for SCC95-IR. SCC96-NR and SCC96-IR exhibit a similar behavior.

5. Conclusion

We have carried out beamtest and β-source measurements for three different designs of thin, 150 μm, n-in-p pixel sensors before and after the irradiation to 2×10^{15} n_{eq}/cm^2 with 23 MeV protons.

The analyses of global hit efficiencies, noise occupancy, charge collection, and the charge collection in depth show consistent full depletion voltages of approximately 50 V and 400 V, before and after irradiation, respectively. The full depletion voltages were estimated to be 44 ± 10 V and 380 ± 70 V, and the effective doping concentration, $(2.6 \pm 0.6) \times 10^{12}$ and $(2.2 \pm 0.4) \times 10^{13}$ cm^{-3}, before and after irradiation, respectively.

The flat distribution of the collected charge in depth after the irradiation implies that the effect of charge trapping in depth is small with the bias voltage well above the full depletion voltage. This is consistent with the estimated charge trapping distance of 150 μm for the fluence of 2×10^{15} n_{eq}/cm^2 which is comparable with the thickness of the sensor.

The common p-stop shows, before and after irradiation, a better performance than the individual p-stop, concerning the hit efficiency. The punch-through design shows, before and after irradiation, a lower efficiency in the region of the implantation dots than the polysilicon bias resistor design.

Due to the low statistics of only two irradiated samples and due to the missing charge calibration for the FE-I4A samples, further measurements are required to confirm the results concerning the different charge collection in the common and the individual p-stop structures, and to understand if there are significant performance differences between the different designs. In order

For an unirradiated sensor with the bias voltage over 50 V and an irradiated one over 500 V, in Fig. 9(d)–(f), we observe a plateau in the collected charge at the inner pixels (depth at ~0.02−0.13 mm) where all pixels collect the same charge. This implies that the effect of charge trapping in depth was small in the irradiated sensors with the present fluence once the bias voltage is well above the full depletion voltage. If we assume a β_e of 3.3×10^{-16}, after annealing and scaled to the temperature at −40 °C, and a fluence of 2×10^{15}, for a saturation drift velocity of 10^7 cm/s, we get a charge trapping distance of approximately 150 μm [11], that is of the order of the sensor thickness, and thus consistent with our observation.

In Fig. 11, we compare the cluster size as a function of the bias voltage for SCC94-NR and SCC95-IR (Fig. 11(a)), and for SCC96-NR and SCC96-IR (Fig. 11(b)). We present the cluster size using a candle stick plot. The solid horizontal line in the middle of each
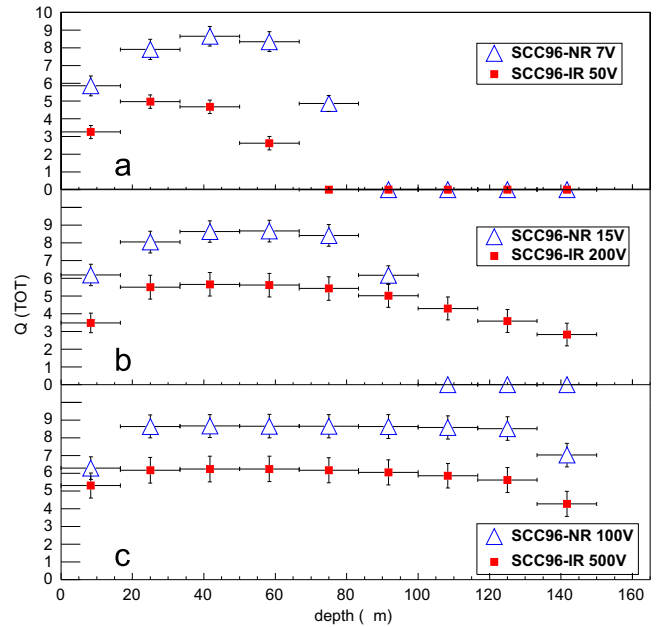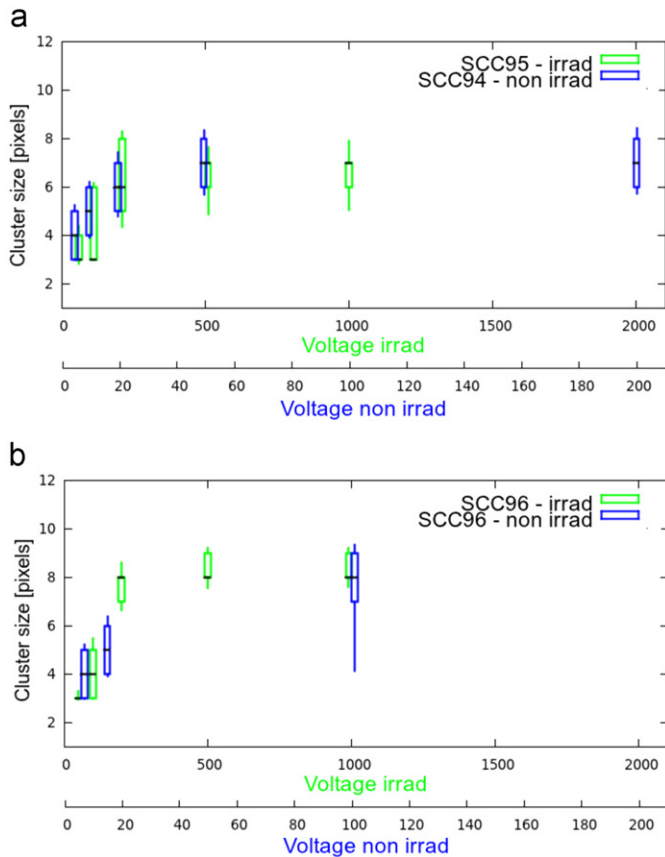
Fig. 11. Comparison of cluster size as a function of the bias voltage using a candle stick plot.

to assure the performance in an environment as the ATLAS pixel detector at the HL-LHC operation, additional irradiation to higher fluences need to be performed in the upcoming years.

Acknowledgments

References

[1] The ATLAS Collaboration, Journal of Instrumentation 3 (2008) S08003.
[2] G. Aad, et al., Journal of Instrumentation 3 (2008) P07007.
[3] C. Da Via, et al., Nuclear Instruments and Methods in Physics Research Section A 604 (2009) 505.
[4] S. Altenheiner, et al., Nuclear Instruments and Methods in Physics Research Section A 658 (2011) 25.
[5] C. Gallrapp, et al., Nuclear Instruments and Methods in Physics Research Section A 679 (2012) 29–35.
[6] P. Weigell, et al., Nuclear Instruments and Methods in Physics Research Section A 658 (2011) 36.
[7] D. Asner, et al., Nuclear Instruments and Methods in Physics Research Section A 636 (2011) S125.
[8] Y. Unno, Nuclear Instruments and Methods in Physics Research Section A 569 (2006) 41.
[9] Y. Unno, et al., Nuclear Instruments and Methods in Physics Research Section A, http://dx.doi.org/10.1016/j.nima.2012.04.061, this issue.
[10] Y. Unno, et al., Nuclear Instruments and Methods in Physics Research Section A 650 (2011) 129.
[11] G. Kramberger, et al., Nuclear Instruments and Methods in Physics Research Section A 481 (2002) 297.
[12] M. Garcia-Sciveres, et al., Nuclear Instruments and Methods in Physics Research Section A 636 (2010) S155.
[13] J. Weingarten, M. Bomben, et al., ATLAS PPS Testbeam Collaboration, July 13–24, September 5–11, 2011.
[14] A. Bulgheroni, et al., Nuclear Instruments and Methods in Physics Research Section A 623 (2010) 399.
[15] K. Nakamura, et al., Journal of Physics G 37 (2010) 075021.